Electronic Supplementary Information

Preparation of a One-Dimensional Hierarchical MnO@CNT@Co-N/C Ternary Nanostructure as a High-Performance Bifunctional Electrocatalyst for Rechargeable Zn-Air Batteries

Fen Li,[a] Tengteng Qin,[a] Yuping Sun,[a] Renjun Jiang,[a] Jiangfeng Yuan,[a] Xiaoqiang Liu*[a] and Anthony P. O'Mullane*[b]

[a] Henan Joint International Research Laboratory of Environmental Pollution Control Materials, College of Chemistry and Chemical Engineering, Henan University, Kaifeng, 475004, PR China.

[b] School of Chemistry and Physics, Queensland University of Technology (QUT), Brisbane, QLD 4001, Australia.

EXPERIMENTAL SECTION

Chemicals and reagents

Potassium permanganate ($KMnO_4$, 99.5%), sodium dodecyl sulfonate ($C_{12}H_{25}NaO_3S$, 99.5%), potassium hydroxide (KOH, 85.0%) and potassium chloride (KCl, 99.5%) were obtained from Tianjin Kemiou Chemical Reagent Co., Ltd, China. Cobalt nitrate hexahydrate ($Co(NO_3)_2 \cdot 6H_2O$, 99.9%), 2-methylimidazole ($C_4H_6N_2$, 98.0%) and zinc acetate ($C_4H_6O_4Zn$, AR) were purchased from Shanghai Macklin Biochemical Technology Co., Ltd, China. Pyrrole (C_4H_5N, 98.0%) was acquired from Sinopharm Chemical Reagents Co. Ltd, China. Commercial 20 w.t.% Pt/C catalyst was ordered from Shanghai Hesen Electric Co., Ltd, China. RuO_2 (99.95%) was purchased from Alfa Aesar (Tianjin) Chemical Co., Ltd. Nafion (5 w.t.%) was bought from Sigma Aldrich (Shanghai) Trading Co., Ltd. Sulfuric acid (H_2SO_4, 98.0 w.t.%) and hydrochloric acid (HCl, 37.0 w.t.%) were purchased from Kaifeng Dongda Chemical Co., Ltd, China. Dehydrated ethanol (C_2H_5OH, 99.7%) and methanol (CH_3OH, 99.5%) were acquired from Anhui Ante Food Co., Ltd, China and Tianjin Fuyu Fine Chemicals

Co. Ltd, China, respectively. Ultrapure water (18.2 MΩ cm) used in all tests was obtained from Millipore water purification system. All the drugs and reagents were used in the experiment without further purification.

Synthesis of materials

Synthesis of MnO_2 nanotubes.

Firstly, 0.658 g $KMnO_4$ was dissolved in 75 mL of ultrapure water and stirred at room temperature for 10 min. Next, 1.5 mL HCl was added to the $KMnO_4$ solution, which was stirred for another 30 min at room temperature. After that, the mixed solution was transferred to a 150 mL Teflon-lined stainless steel autoclave, which was then placed in an oven at 150 °C for 12 h. After being neutralized and cooled to ambient temperature, the brown precipitate was collected by centrifugation (10000 rpm, 3 min), washed with ultrapure water and dehydrated ethanol for three times, and dried in an electronic oven at 60 °C for 24 h to obtain the final product of MnO_2 nanotubes.

Synthesis and surface treatment of MnO_2@PPy coaxial nanotubes.

Firstly, 0.15 g of MnO_2 nanotubes was dispersed in 60 mL of 0.01 M H_2SO_4 solution and sonicated for 30 min to obtain a uniform dispersion, which was then stirred in an ice bath for 30 min. Next, 0.01 M H_2SO_4 (40 mL) solution containing 0.1 mL pyrrole monomer was rapidly added to the above dispersion under continuous stirring, and then a dark brown flocculent precipitate appeared immediately. The mixture was continuously stirred in ice bath for 3 h, and then centrifuged. The obtained MnO_2@PPy precipitate was washed with ultrapure water and dehydrated ethanol for three times successively, finally dried at 60 °C for 12 h.

To modify a surfactant on the surface of MnO_2@PPy composite, an appropriate amount of sodium dodecyl sulfonate was dissolved in 30 mL ultrapure water, and then 80 mg of MnO_2@PPy coaxial nanotubes and 40 mL of methanol were added. The mixed solution was sonicated for 3 h and then centrifuged. The precipitate was collected, washed with methanol for 4 times, and dried in an oven at 80 °C for 7 h to obtain the final product, defined as MnO_2@PPy-S.

Synthesis of MnO_2@PPy@ZIF-67 and MnO@CNT@Co-N/C.

Firstly, 60 mg of MnO_2@PPy-S and 0.2911 g of $Co(NO_3)_2 \cdot 6H_2O$ were ultrasonically dispersed in 50 mL of methanol for 3 h to form a uniform dispersion. Meanwhile, 0.6568 g of 2-methylimidazole was dissolved in 30 mL of methanol to form a clear solution. Under vigorous stirring, 2-methylimidazole solution was quickly added to the above dispersion to immediately obtain a dark purple solution, which was continually stirred for 1 h and then left standing for 24 h. The final product of MnO_2@PPy@ZIF-67 was obtained by centrifugalization with methanol for 4 times and then dried in an oven at 80 °C for 7 h. After that, MnO_2@PPy@ZIF-67 was placed in a tube furnace and calcined at 700 °C for 4 h under Ar atmosphere at a heating rate of 5 °C min^{-1} to yield MnO@CNT@Co-N/C.

Characterization

Powder X-ray diffraction (XRD) patterns were collected on a Bruker D8 Advance X-ray diffractometer (Bruker, Germany) with Cu Kα radiation (λ = 1.5406 nm). X-ray photoelectron spectroscopic (XPS) measurements were conducted on a ESCALAB 250Xi spectrometer made by ThermoFisher, USA and equipped with a monochromated Al Kα source (hν = 1486.6 eV), 150 W power and 500 μm beam spot. The collected spectra were calibrated via the C 1s peak (284.8 eV) and analyzed using the XPSPEAK41 software. Fourier transform infrared spectroscopy (FT-IR) measurements were collected on a VERTEX 70 device from BRUKER OPTICS Corporation in Germany. Field emission scanning electron microscopy (SEM) images were collected on a Carl Zeiss Gemini500 from England. The transmission electron microscope (TEM) and lattice fringe images were collected on a FEI Tecnai G2 F30 TEM equipped with an energy-dispersive X-ray (EDX) detector. Raman scattering spectra were captured on a Renishaw inVia spectrometer (United Kingdom) with an excitation wavelength of 532 nm. N_2 adsorption/desorption isotherm was obtained using a specific surface and porosity analyzer (Quadrasorb SI-4, USA) at a liquid nitrogen temperature of 77 K after the sample was pretreated at 300 °C in vacuum for 12 h. The Brunauere–Emmette–Teller (BET) and Barrett–Joyner–Halenda (BJH) models were used to calculate the specific surface area and pore size of the MnO@CNT@Co-N/C, respectively. Electrochemical impedance spectroscopy (EIS) was carried out on a potentiostat (Zahner, Germany).

Electrochemical measurements

All electrochemical measurements were performed on a CHI730E electrochemical workstation (CH Instruments, Shanghai, China) equipped with a standard three-electrode system consisting of a catalyst-coated glassy carbon rotating disk electrode (RDE, 3 mm in diameter) or rotating ring-disk electrode (RRDE, disk area: 0.1257 cm^2, Pt ring area: 0.1885 cm^2) as the working electrode, a Hg/HgO (in 1 M KOH solution) electrode as the reference electrode and a Pt wire as the counter electrode. The potentials of all measurements were converted into the values versus a reversible hydrogen electrode (RHE) according to the formula：

$$E_{vs.\ RHE} = E_{vs.\ Hg\ /\ HgO} + 0.098\ V + 0.059 \times pH\ (0.1\ M\ KOH)$$

To prepare a catalyst modified working electrode, firstly, 3.5 mg of catalyst powder was initially dispersed in a mixed solution consisted of 870 μL of absolute ethanol, 100 μL of high purity water and 30 μL of 5% Nafion, and ultrasonically treated for 1 h until a stable and uniform slurry was formed. Then, a certain volume of catalyst slurry was applied onto a RDE or RRDE, and dried to obtain a modified working electrode with a catalyst load of 0.4 mg cm^{-2}. For comparison, the commercial 20 w.t. % Pt/C and RuO_2 catalysts modified electrodes were prepared with the same procedure.

For oxygen reduction reaction (ORR), cyclic voltammetry (CV) tests were carried out in a N_2 or O_2-saturated 0.1 M KOH solution at a sweep rate of 50 $mV \cdot s^{-1}$, and linear sweep voltammetry (LSV) was measured in O_2-saturated 0.1 M KOH solution at a sweep speed of 10 $mV \cdot s^{-1}$ with different rotation rates (the current density has been corrected by the blank under N_2 unless otherwise specified). For oxygen evolution reaction (OER), LSV was performed in an O_2-saturated 0.1 M KOH solution at a sweep speed of 5 $mV \cdot s^{-1}$ with a fixed rotation rate of 1600 rpm. Chronoamperometric test was performed in an O_2-saturated electrolyte at 0.67 V at 1600 rpm to evaluate the stability and methanol tolerance of the catalysts.

Electrochemically active surface area (ECSA) was evaluate based on the double-layer capacitance (C_{dl}) obtained from the cyclic voltammograms (CV) at different scan rates from 1 to 10 mV s^{-1} in non-Faradaic region from 1.18 to 1.28 V (*vs* RHE). The half of absolute current density variation ($|j_a - j_c|/2$) at 1.23 V versus scan rates was

plotted and the slope of the plot is C_{dl}, which is proportional to the ECSA according to the following equation:

$$ECSA = C_{dl}/C_s$$

where C_s is the specific capacitance value of a smooth surface of materials under specific electrochemical condition.

Koutecky–Levich (K–L) plots of ORR under 0.4-0.6 V voltage were obtained from the K-L equation as follows:

$$\frac{1}{J} = \frac{1}{J_L} + \frac{1}{J_K} = \frac{1}{B\omega^{1/2}} + \frac{1}{J_K}$$

where J, J_K and J_L represent the measured current density, kinetics and diffusion limiting current density, respectively, and ω is the rotation speed (rpm) of the electrode. The slope and intercept of the K–L plot equals to 1/B and $1/J_K$, respectively. Therefore, the ORR electron transfer number (n) could be theoretically calculated according to the following equation:

$$B = 0.2nFC_0(D_0)^{2/3}\upsilon^{-1/6}$$

where F is the Faraday constant (F = 96485 C mol^{-1}), C_0 is the volume concentration of O_2 (C_0 = 1.2 × 10^{-6} mol cm^{-3}), D_0 is the O_2 diffusion coefficient in 0.1 M KOH (D_0 = 1.9 × 10^{-5} cm^2 s^{-1}), υ is the kinematic viscosity of the electrolyte (υ = 0.01 cm^2 s^{-1}).

According to the RRDE experiments at 1600 rpm, the electron transfer number in ORR and the percentage of peroxide can also be calculated from the experimental results using the equations given below:

$$n = \frac{4\, I_{Disk}}{I_{Disk} + I_{Ring}/N}$$

$$\%H_2O_2 = 100 \times \frac{2\, I_{Disk}/N}{I_{Disk} + I_{Ring}/N}$$

where I_{Disk} and I_{Ring} represent disk and ring current respectively, N = 0.424 is current collection efficiency of the Pt ring, $\%H_2O_2$ is the H_2O_2 produced during the ORR reaction.

Zn-Air Battery Test

A primary liquid Zn-Air battery consists of an air cathode, a polished zinc plate (0.5 mm thickness) as the anode, a separator, and a mixture solution of 6 M KOH+ 0.2 M $Zn(Ac)_2$ as the electrolyte. To prepare the catalyst slurry for air cathode, 10 mg of MnO@CNT@Co-N/C and commercial Pt/C+RuO_2 [20 w.t.% Pt/C : RuO_2 (Alfa Aesar, 99.95%) = 1 : 1] catalysts were respectively dispersed in a solution composed of 950 μL anhydrous ethanol and 50 μL 5% Nafion under 1 h of ultrasonic. Then, 157 μL of the obtained uniform slurry was cast on the carbon paper side of a composite substrate (carbon paper + waterproof film + nickel foam) (1 cm in diameter) and dried overnight in a 40 °C electronic oven to obtain a final average loading of 2 mg cm^{-2}. Then this catalyst modified substrate was used as the air cathode in the Zn-air battery. All the battery tests were performed at room temperature in this work. The charge-discharge polarization curves of MnO@CNT@Co-N/C and Pt/C+RuO_2 catalysts were collected at a sweep rate of 5 mV s^{-1} using LSV technique on a CHI760E electrochemical workstation. Cyclic stability test of the battery was carried out at a constant current density of 5 mA cm^{-2} with 20 min of each cycle consisting of 10 min of discharge and 10 min of charge on LANHE CT3002A test system. The current density and power density used in the experiment are normalized by the effective area of the air electrode. The galvanostatic method was used to collect the constant current discharge curve by discharging at a constant current density of 5 mA cm^{-2}. Then, the normalized specific capacity and energy density were calculated according to the following equations:

$$\text{Specific capacity (mAh g}^{-1}) = I \times t / W_{Zn}$$

$$\text{Energy density (Wh kg}^{-1}) = I \times V \times t / W_{Zn}$$

where I, V, t and W_{Zn} represent the applied constant current, average discharge voltage, serving time, and consumed weight of the zinc plate, respectively.

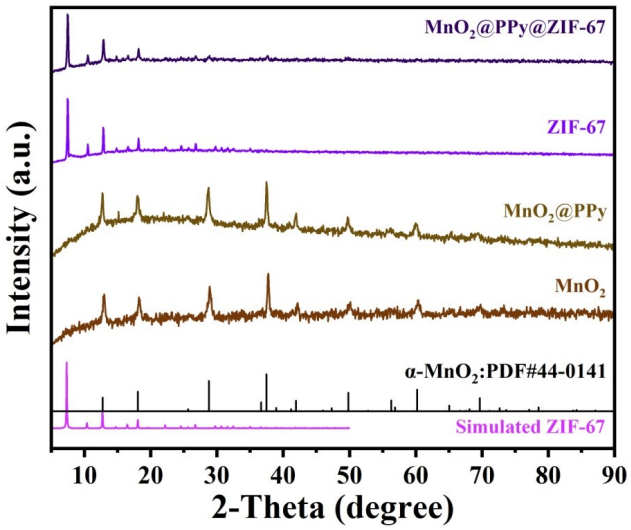

Fig. S1 XRD patterns of MnO_2, MnO_2@PPy, ZIF-67, and MnO_2@PPy@ZIF-67.

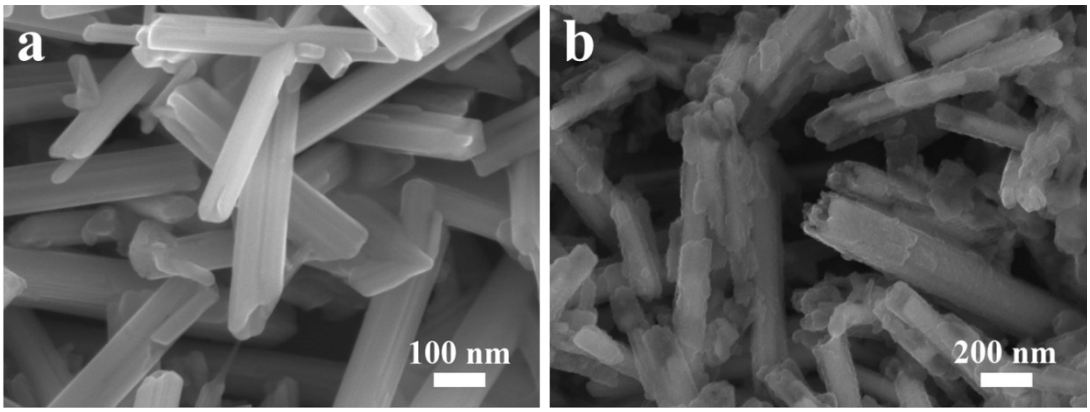

Fig. S2 SEM images of (a) MnO_2 nanotubes and (b) MnO_2@PPy coaxial nanotubes.

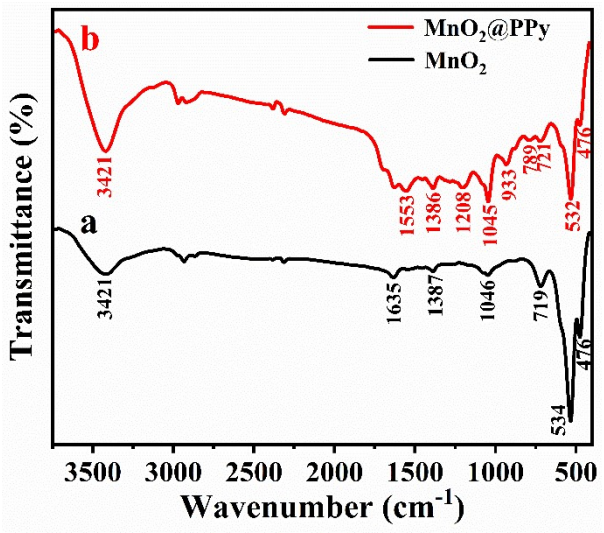

Fig. S3 FT-IR spectrum of MnO_2 nanotubes and MnO_2@PPy coaxial nanotubes.

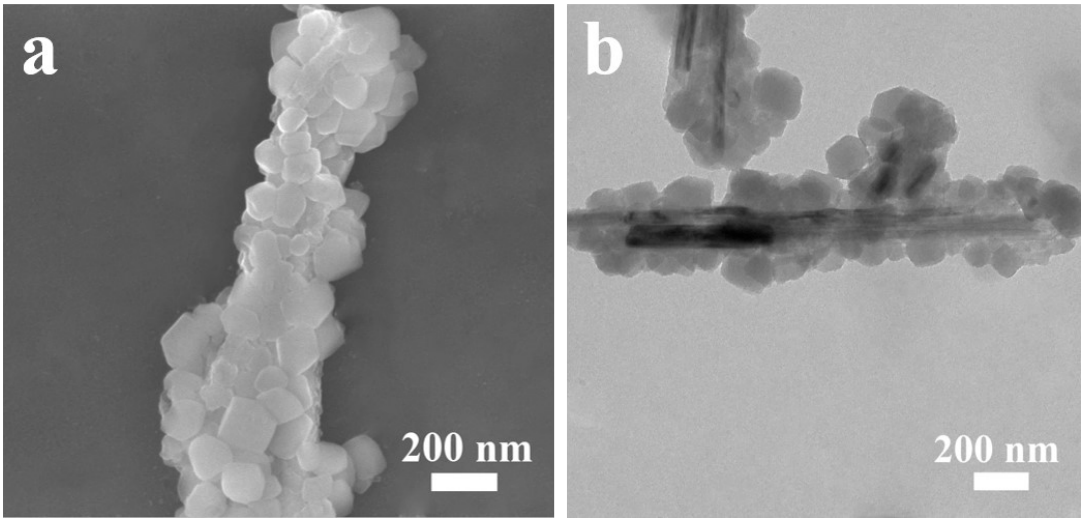

Fig. S4 (a) SEM and (b) TEM images of MnO_2@PPy@ZIF-67.

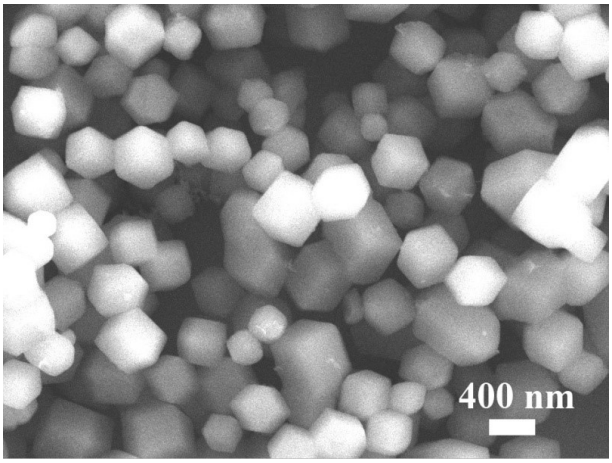

Fig. S5 SEM image of ZIF-67.

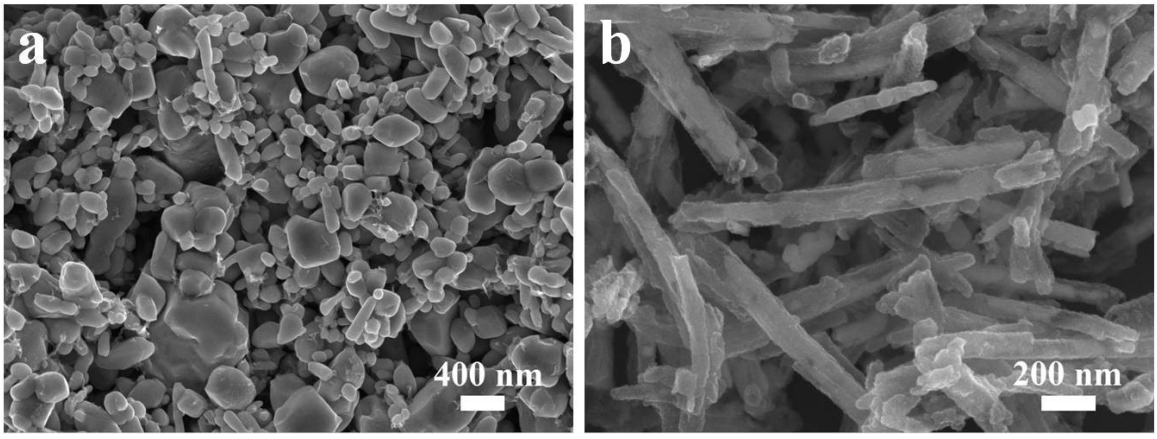

Fig. S6 SEM images of (a) MnO derived from pure MnO_2 NTs and (b) MnO@CNT.

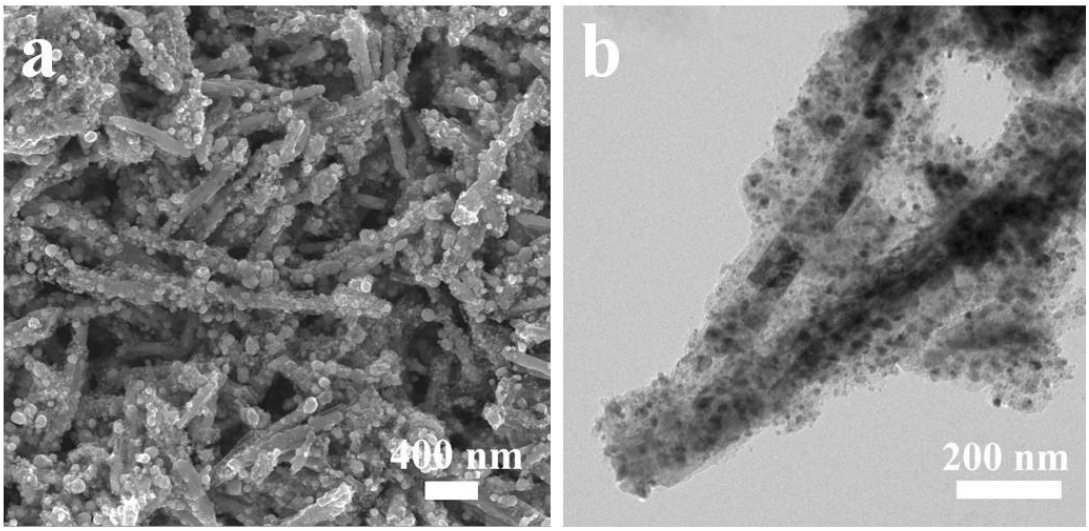

Fig. S7 (a) SEM and (b) TEM images of MnO@CNT@Co-N/C.

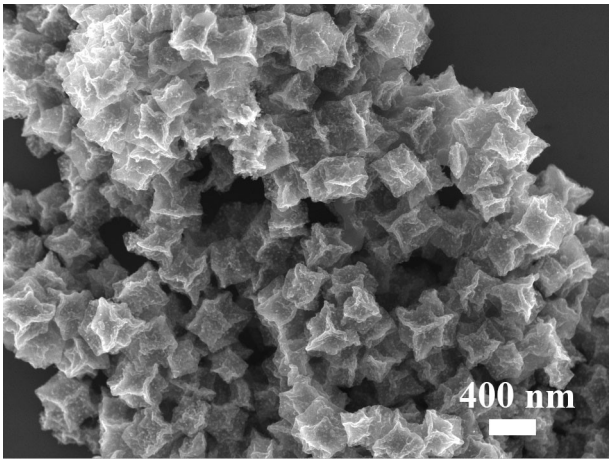

Fig. S8 SEM image of Co-N/C derived from ZIF-67.

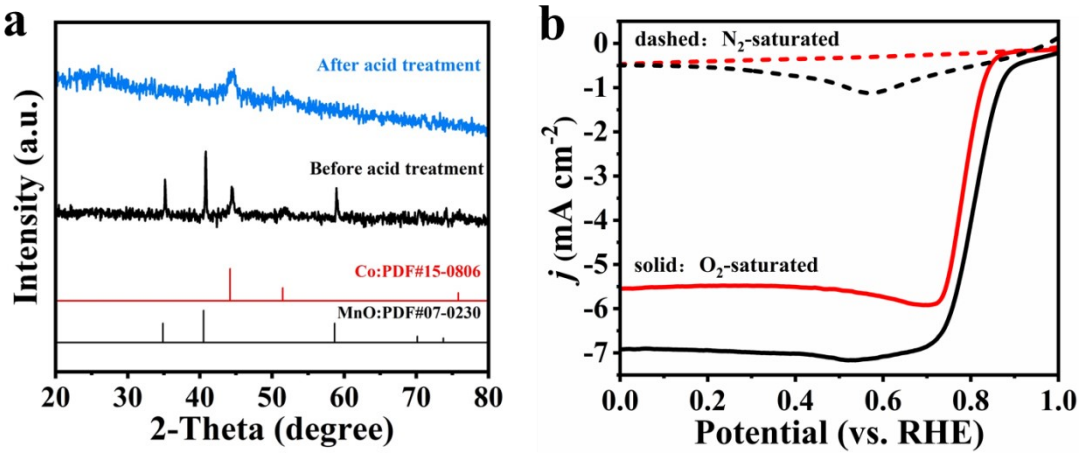

Fig. S9 (a) XRD patterns of MnO@CNT@Co-N/C before and after acid treatment. (b) ORR LSV curves of MnO@CNT@Co-N/C before (black curves) and after (red curves) acid treatment in N_2 (dashed) or O_2-saturated (solid curves) 0.1 M KOH at 1600 rpm-current density without correction by the blank under N_2.

To better verify the function of MnO for the ORR performance of MnO@CNT@CoN/C, the calcined product was initially treated with 1 M HCl overnight. As confirmed by the XRD patterns (Fig. S9a), only the characteristic peaks of MnO disappeared after the acid treatment, while the characteristic peaks from the other components still exist and their peak intensities are nearly same as those before acid treatment, indicating successful elimination of MnO from MnO@CNT@Co-N/C with acid. Then, LSV curves of MnO@CNT@CoN/C before and after acid treatment were obtained to verify the role of MnO for the ORR performance of MnO@CNT@Co-N/C. The LSV diagram (Fig. S9b) clearly indicated the ORR catalytic performance (E_{onset}, $E_{1/2}$ and J_L) of the material was significantly weakened after acid treatment, which is highly likely due to the elimination of MnO from the composite. In addition, the obvious voltammetry peak at ~ 0.55 V on LSV curve also vanished, implying that this peak belongs to MnO. The above test results demonstrate that MnO plays an important role in synergistically improving the ORR performance together with the other components in the composite.

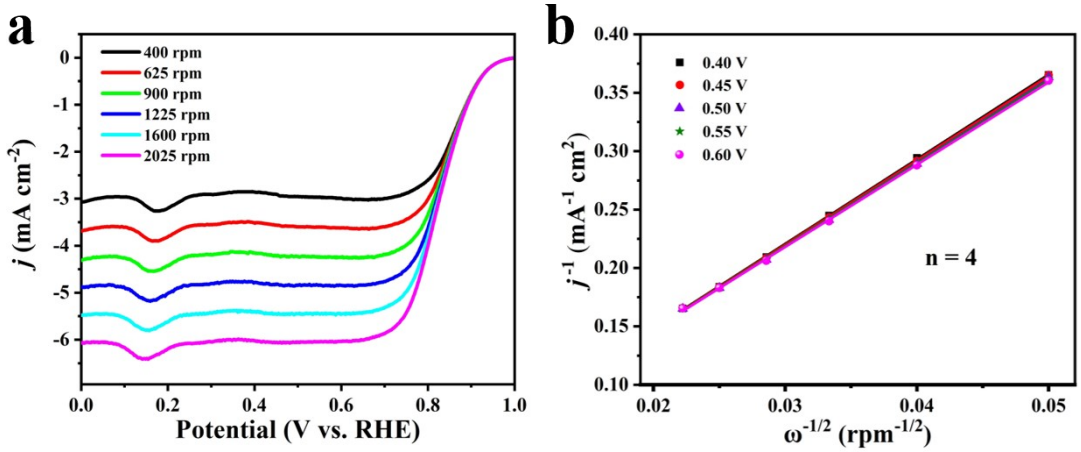

Fig. S10 (a) LSV curves of Pt/C in O_2-saturated 0.1 M KOH electrolyte at a scan rate of 10 mV s^{-1} with different rotation rates. (b) K-L plots of Pt/C at different potentials.

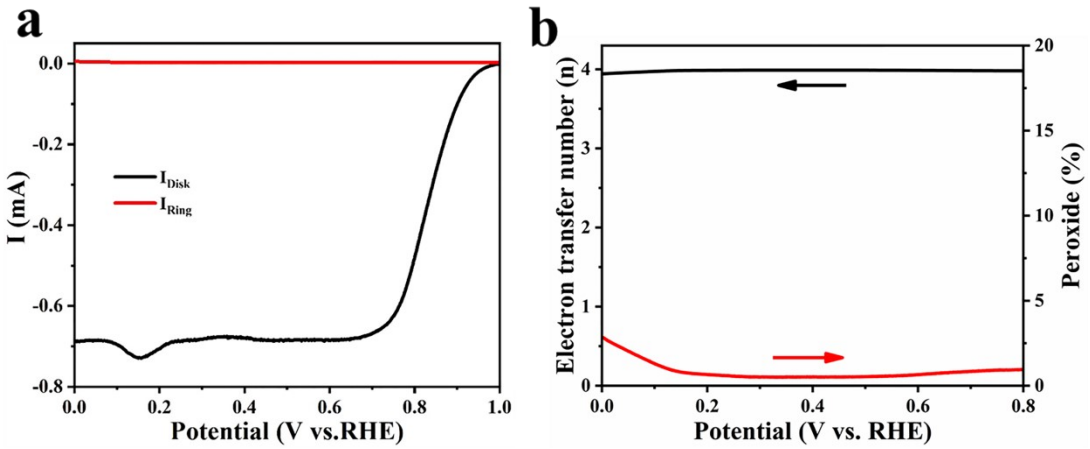

Fig. S11 (a) The Ring current and Disk current curves of Pt/C at 1600 rpm measured by RRDE. (b) Electron transfer numbers (n) and percentage of peroxide of Pt/C at various potentials.

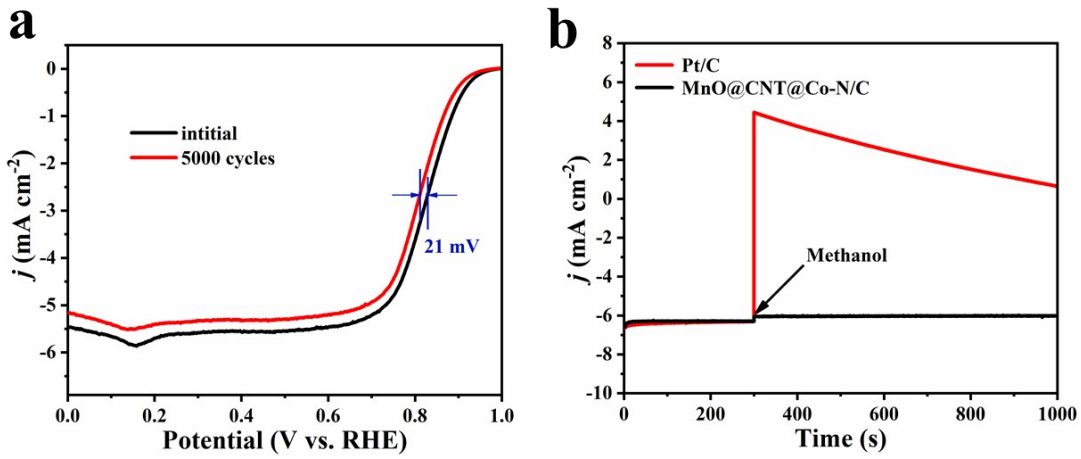

Fig. S12 (a) LSV curves of Pt/C before and after 5000 cycles of continuous CV scan in O_2-saturated 0.1 M KOH electrolyte. (b) Methanol tolerance test by injecting 1 M methanol to 0.1 M KOH at 300 s.

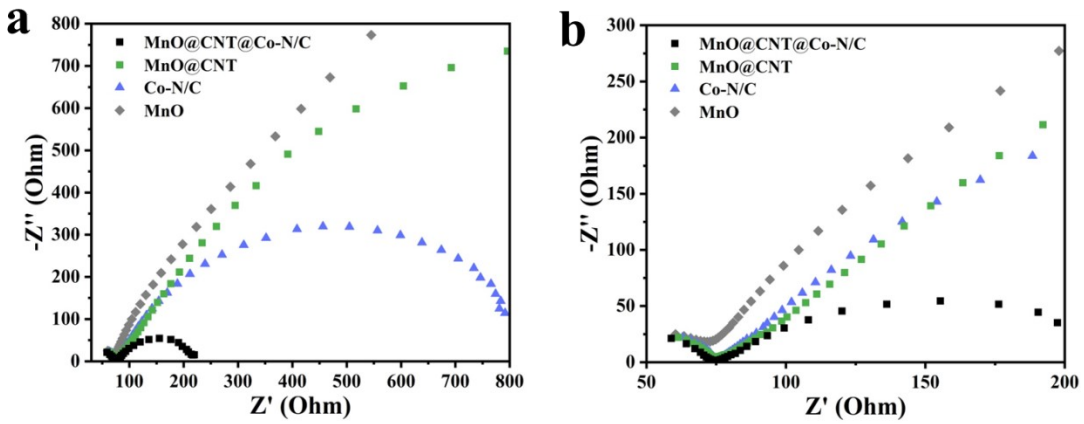

Fig. S13 EIS of different catalysts in O_2-saturated 0.1M KOH at the potential of 1.60 V.

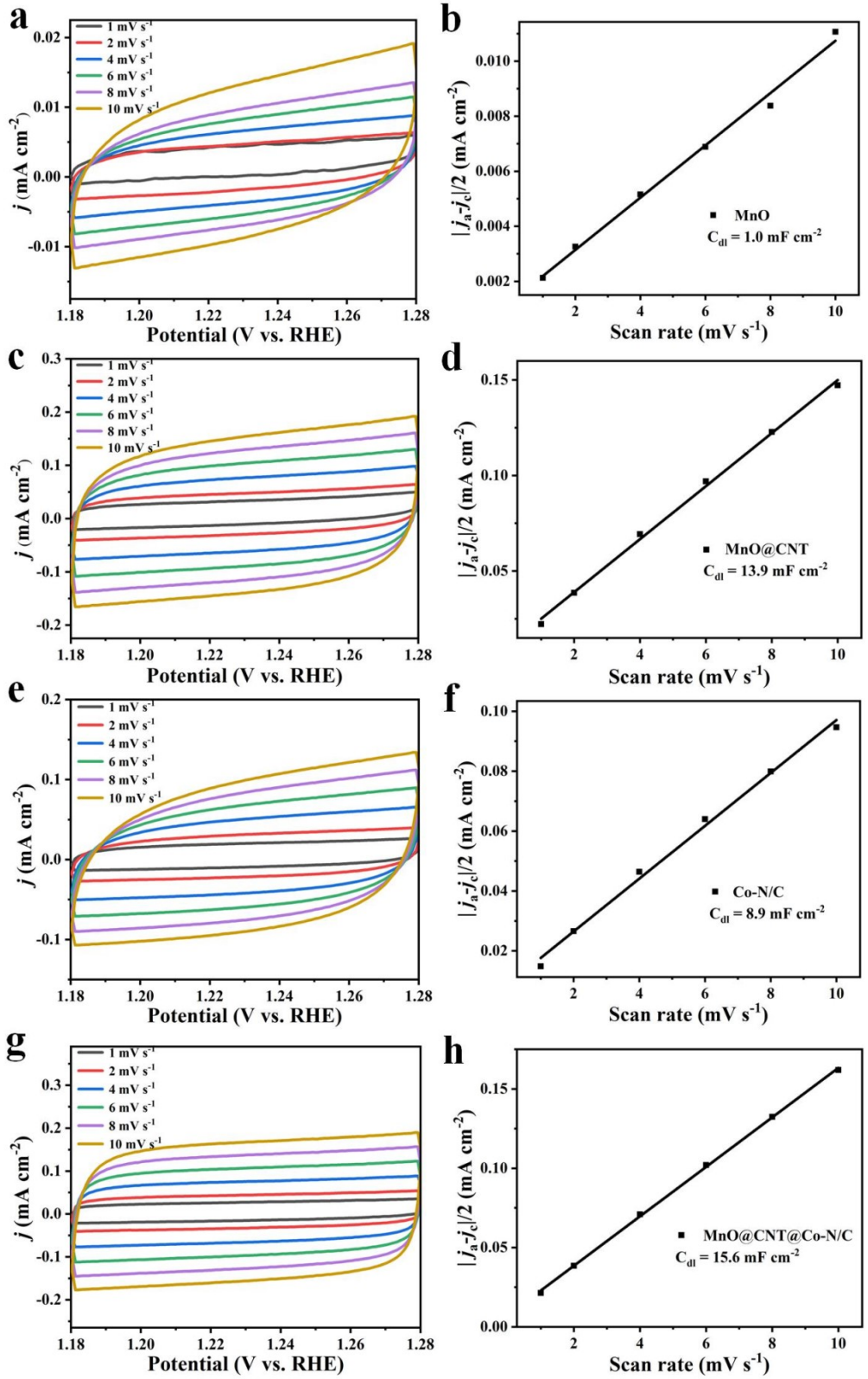

Fig. S14 CV curves at different scan rates and corresponding double-layer capacitance (C_{dl}) of the (a, b) MnO; (c, d) MnO@CNT; (e, f) Co-N/C and (g, h) MnO@CNT@Co-N/C catalysts.

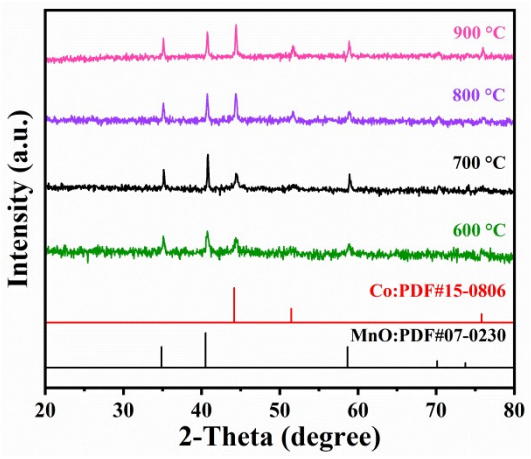

Fig. S15 XRD patterns of MnO@CNT@Co-N/C at different pyrolysis temperature.

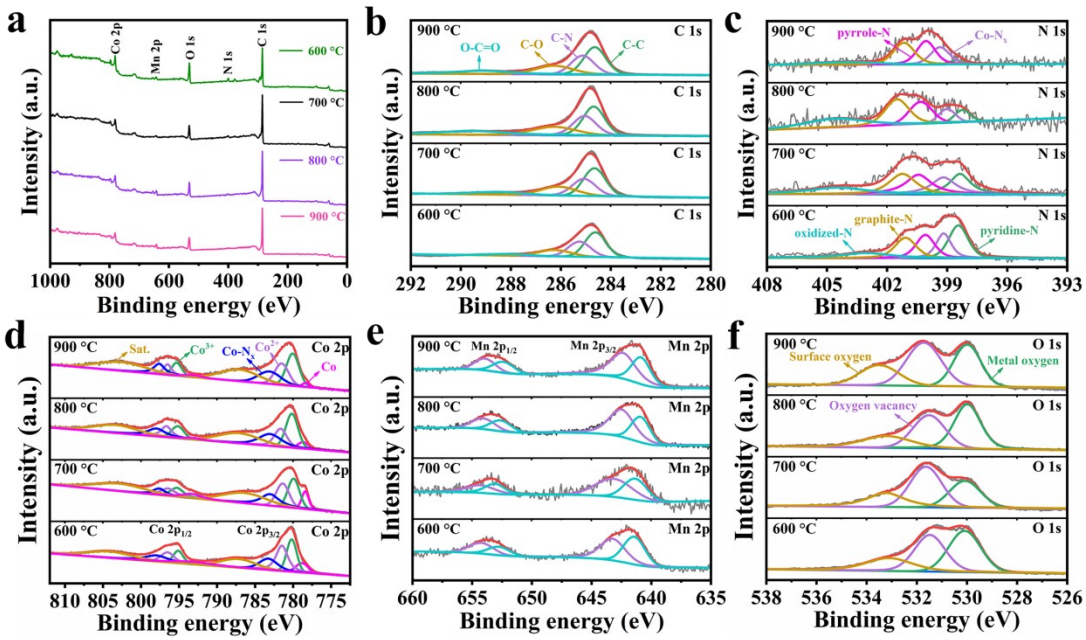

Fig. S16 (a) Survey scan, (b) C 1s, (c) N 1s, (d) Co 2p, (e) Mn 2p and (f) O 1s XPS spectra of MnO@CNT@Co-N/C at different pyrolysis temperature.

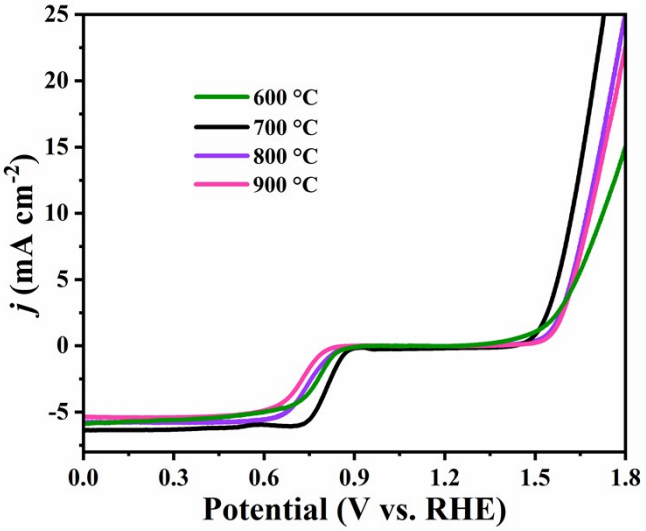

Fig. S17 The overall ORR and OER polarization curves of MnO@CNT@Co-N/C calcined at different temperatures.

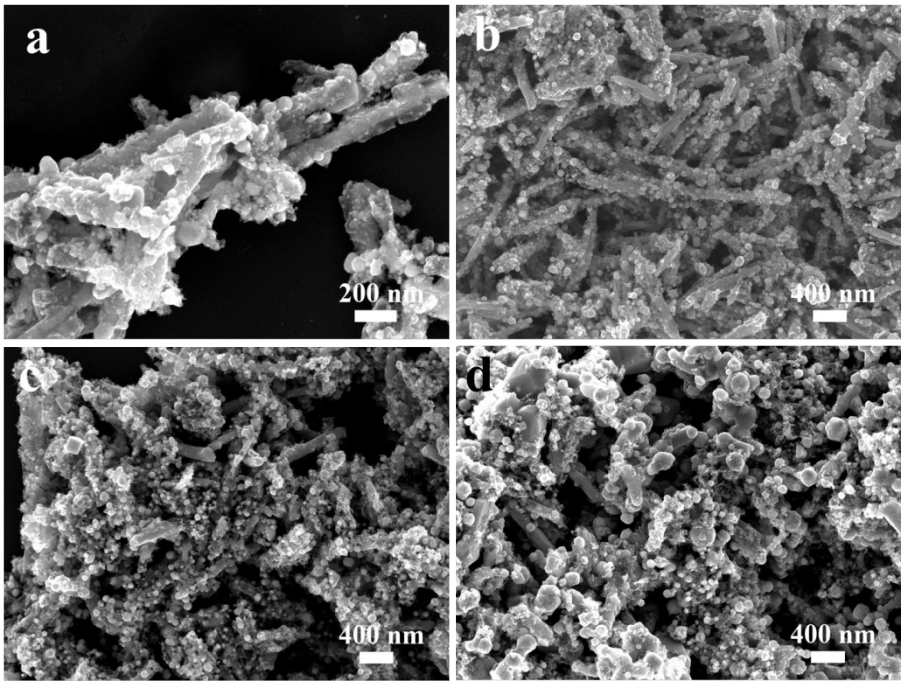

Fig. S18 The SEM images of MnO@CNT@Co-N/C calcined at (a) 600 ℃, (b) 700 ℃, (c) 800 ℃ and (d) 900 ℃.

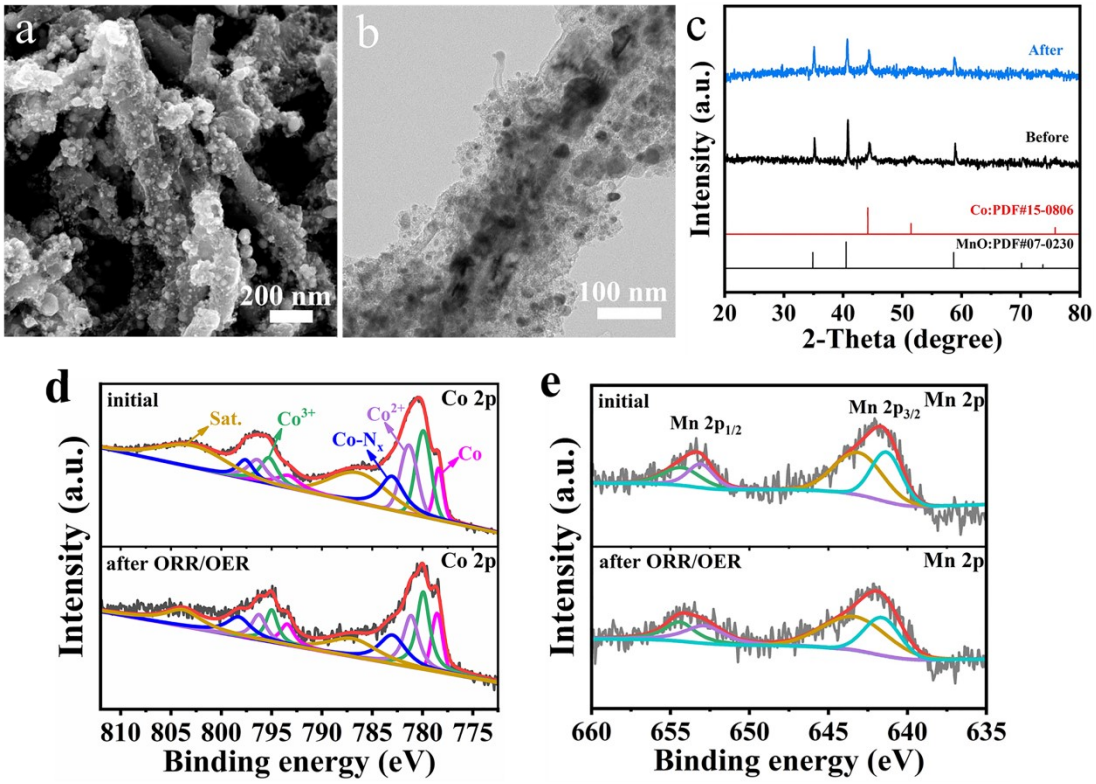

Fig. S19 (a) SEM, (b) TEM images and (c) XRD patterns of MnO@CNT@Co-N/C after the durability test. (d) High-resolution Co 2p and (e) Mn 2p XPS spectra of MnO@CNT@Co-N/C before and after ORR/OER test.

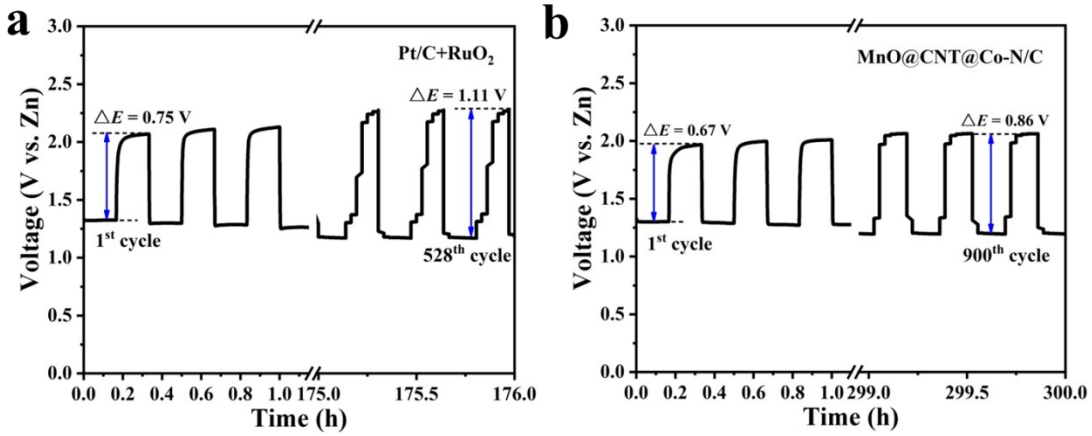

Fig. S20 The discharge-charge voltage gap curves of the first and last cycle of Zn-air battery with (a) Pt/C+RuO_2 and (b) MnO@CNT@Co-N/C as the air electrode catalyst, respectively.

Table S1 N1s peak fitting results of the samples pyrolysis at different temperatures.

Samples	Total-N (%)	pyridine -N (%)	Co-N_x (%)	pyrrole-N (%)	graphite-N (%)	Oxidized-N (%)
MnO@CNT@ Co-N/C-600	6.6	27.63	17.99	20.18	19.83	14.37
MnO@CNT@ Co-N/C-700	3.22	18.95	18.60	22.89	21.80	17.76
MnO@CNT@ Co-N/C-800	1.99	8.55	10.17	22.92	31.29	27.07
MnO@CNT@ Co-N/C-900	1.7	4.02	22.25	30.89	32.63	10.21

Table S2 Comparison of bifunctional activities for different catalysts.

Catalyst	ORR		OER		ΔE (V)	Ref.
	E_{onset} (V)	$E_{1/2}$ (V)	E_{onset} (V)	$E_{j=10}$ (V)		
MnO@CNT@Co-N/C	**0.93**	**0.81**	**1.51**	**1.62**	**0.81**	**This work**
CoNP-PTCOF [a]	\	0.85	\	1.68	0.83	1
Co@Co_3O_4/NC	0.91	0.8	\	1.65	0.85	2
Co_3O_4/NHPC [b]	0.96	0.835	\	1.65	0.815	3
nano-$MnCo_2O_{4.5}$	0.82	0.72	1.62	1.64	0.92	4
MnOx/NC [c]	0.95	0.80	1.41	1.67	0.87	5
CoFe/N-GCT [d]	0.91	0.79	1.54	1.67	0.88	6
rGO/CB_2/Co-B_i [e]	0.88	0.7	1.52	1.57	0.87	7
HNG [f]-900	\	0.78	\	1.69	0.91	8
$MnCo_2O_4$/NGr [g]	0.93	0.85	\	1.76	0.91	9
$Co_3FeS_{1.5}(OH)_6$	\	0.72	\	1.59	0.87	10
$Zn_{0.4}Ni_{0.6}Co_2O_4$/NCNTs	\	0.78	\	1.64	0.86	11
Hybrid nanosheets	0.90	0.79	\	1.723	0.933	12
Co_9S_8/GN [h]-0.02	0.93	0.8	\	1.68	0.88	13
Co-MOF-800	\	0.84	\	1.75	0.84	14
Co-POC [i]	\	0.83	\	1.70	0.87	15

[a] pyridine-linked triazine covalent organic framework
[b] nitrogen-doped hierarchically porous carbon
[c] N-doped carbon
[d] N-doped 3D carbon matrix composed of graphene interconnected with carbon nanotubes
[e] reduced graphene oxide/carbon black/amorphous cobalt borate nanocomposites
[f] holey N-doped grapheme
[g] nitrogen-doped reduced graphene oxide
[h] graphene nanosheet
[i] cobalt-coordinated framework porphyrin with graphene

Table S3 Performance comparison of Zn-Air batteries with different catalysts.

Catalyst	OCV (V)	Peak power density (mW cm^{-2})	Special capacity (mAh g^{-1})	Energy density (Wh kg^{-1})	Cycling conditions	Ref.
MnO@CNT@Co-N/C	**1.45**	**200.8**	**802.7**	**1010.6**	**5 mA cm^{-2}, 20 min/cycle for 900 cycles (300 h)**	**This work**
Pt/C+RuO_2	**1.42**	**136.9**	**748.2**	**914.4**	**5 mA cm^{-2}, 20 min/cycle for 528 cycles (176 h)**	**This work**
CoO_x@NGCR [j]	1.40	90.1	\	\	5 mA cm^{-2}, 20 min/cycle for 50 cycles (16.7 h);	16
CoNCF [k]-1000-80	1.44	170.0	650.0	797.0	10 mA cm^{-2}, 20 min/cycle for 500 cycles	17
$CoFe_{20}$@CC	1.50	190.3	787.9	1012.0	5 mA cm^{-2}, 20 min/cycle for 400 cycles	18
MnO-Co@NC	1.40	86.0	\	\	5 mA cm^{-2}, 5 min/cycle for 180 cycles	19
NCNT/MnO-$(MnFe)_2O_3$	1.45	\	647.0	776.0	20 mA cm^{-2}, 10 min/cycle for 133 cycles	20
Co_3O_4/N-CNTAs [l]	\	\	597.0	734.0	5 mA cm^{-2}, 10 min/cycle for 100 cycles (16.7 h)	21
In-CoO/CoP FNS [m]	1.40	139.4	739.0	938.0	10 mA cm^{-2}, 40 min/cycle for 205 cycles (136 h)	22
Co-MOF	1.33	86.2	\	\	6 mA cm^{-2}, 20 min/cycle for 220 cycles (73 h)	23
N-$CoSe_2$/3D $Ti_3C_2T_x$	1.43	142.0	751.0	903.0	5 mA cm^{-2}, 20 min/cycle for 500 cycles (166 h)	24
Pt-SCFP [n]/C-12	1.40	122.0	\	790.4	5 mA cm^{-2}, 20 min/cycle for 240 cycles	25

[j] CoO_x nanoparticles (CoO_x NPs) situated in N-doped graphitic carbon nanorings
[k] cobalt nanoparticles confined in 3D nitrogen-doped porous carbon foams
[l] nitrogen-doped carbon nanotube arrays
[m] In-doped CoO/CoP heterostructure
[n] $Sr(Co_{0.8}Fe_{0.2})_{0.95}P_{0.05}O_{3-\delta}$

References

1 J. H. Park, C. H. Lee, J. M. Ju, J. H. Lee, J. Seol, S. U. Lee and J. H. Kim, *Adv. Funct. Mater.*, 2021, 2101727.

2 A. Aijaz, J. Masa, C. Rosler, W. Xia, P. Weide, A. J. Botz, R. A. Fischer, W. Schuhmann and M. Muhler, *Angew. Chem. Int. Ed.*, 2016, **55**, 4087-4091.

3 J. Guan, Z. Zhang, J. Ji, M. Dou and F. Wang, *ACS Appl. Mater. Interfaces*, 2017, **9**, 30662-30669.

4 Z. Bai, J. Heng, Q. Zhang, L. Yang and F. Chang, *Adv. Energy Mater.*, 2018, **8**, 1802390.

5 J. Pandey, B. Hua, W. Ng, Y. Yang, K. van der Veen, J. Chen, N. J. Geels, J.-L. Luo, G. Rothenberg and N. Yan, *Green Chem.*, 2017, **19**, 2793-2797.

6 X. Liu, L. Wang, P. Yu, C. Tian, F. Sun, J. Ma, W. Li and H. Fu, *Angew. Chem. Int. Ed.*, 2018, **57**, 16166-16170.

7 J. Sun, D. Yang, S. Lowe, L. Zhang, Y. Wang, S. Zhao, P. Liu, Y. Wang, Z. Tang, H. Zhao and X. Yao, *Adv. Energy Mater.*, 2018, **8**, 1801495.

8 H. Cui, M. Jiao, Y.-N. Chen, Y. Guo, L. Yang, Z. Xie, Z. Zhou and S. Guo, *Small Methods*, 2018, **2**, 1800144.

9 A. Qaseem, F. Chen, C. Qiu, A. Mahmoudi, X. Wu, X. Wang and R. L. Johnston, *Part. Part. Syst. Charact.*, 2017, **34**, 1700097.

10 H. F. Wang, C. Tang, B. Wang, B. Q. Li and Q. Zhang, *Adv. Mater.*, 2017, **29**, 1702327.

11 X. T. Wang, T. Ouyang, L. Wang, J. H. Zhong and Z. Q. Liu, *Angew. Chem.*, 2020, **132**, 6554-6561.

12 Y. Li, C. Zhong, J. Liu, X. Zeng, S. Qu, X. Han, Y. Deng, W. Hu and J. Lu, *Adv. Mater.*, 2018, **30**, 1703657.

13 X. Sun, Q. Gong, Y. Liang, M. Wu, N. Xu, P. Gong, S. Sun and J. Qiao, *ACS Appl. Mater. Interfaces*, 2020, **12**, 38202-38210.

14 X. Duan, N. Pan, C. Sun, K. Zhang, X. Zhu, M. Zhang, L. Song and H. Zheng, *J. Energy Chem.*, 2021, **56**, 290-298.

15 B. Q. Li, C. X. Zhao, S. Chen, J. N. Liu, X. Chen, L. Song and Q. Zhang, *Adv. Mater.*, 2019, **31**, 1900592.

16 C.-C. Weng, J.-T. Ren, Z.-P. Hu and Z.-Y. Yuan, *ACS Sustainable Chem. Eng.*, 2018, **6**, 15811-15821.

17 H. Jiang, Y. Liu, W. Li and J. Li, *Small*, 2018, **14**, 1703739.

18 C. C. Hou, L. Zou and Q. Xu, *Adv. Mater.*, 2019, **31**, 1904689.

19 A. Samanta, B. K. Barman, S. Mallick and C. R. Raj, *ACS Appl. Energy Mater.*, 2020, **3**, 10108-10118.

20 Q. Qin, P. Li, L. Chen and X. Liu, *ACS Appl. Mater. Interfaces*, 2018, **10**, 39828-39838.

21 W. Tian, H. Li, B. Qin, Y. Xu, Y. Hao, Y. Li, G. Zhang, J. Liu, X. Sun and X. Duan, *J. Mater. Chem. A*, 2017, **5**, 7103-7110.

22 W. Jin, J. Chen, B. Liu, J. Hu, Z. Wu, W. Cai and G. Fu, *Small*, 2019, **15**, 1904210.

23 G. Chen, J. Zhang, F. Wang, L. Wang, Z. Liao, E. Zschech, K. Mullen and X. Feng, *Chem. Eur. J.*, 2018, **24**, 18413-18418.

24 Z. Zeng, G. Fu, H. B. Yang, Y. Yan, J. Chen, Z. Yu, J. Gao, L. Y. Gan, B. Liu and P. Chen, *ACS Materials Lett.*, 2019, **1**, 432-439.

25 X. Wang, J. Sunarso, Q. Lu, Z. Zhou, J. Dai, D. Guan, W. Zhou and Z. Shao, *Adv. Energy Mater.*, 2020, **10**, 1903271.